

Article

# A Burned Area Mapping Algorithm for Chinese FengYun-3 MERSI Satellite Data

Tianchan Shan <sup>1,2</sup>, Changlin Wang <sup>1</sup>, Fang Chen <sup>1,2,3,\*</sup>, Qinchun Wu <sup>1,2</sup>, Bin Li <sup>1</sup>, Bo Yu <sup>1</sup>, Zeeshan Shirazi <sup>1,2</sup>, Zhengyang Lin <sup>1,2</sup> and Wei Wu <sup>1,2</sup>

<sup>1</sup> Key Laboratory of Digital Earth Science, Institute of Remote Sensing and Digital Earth, Chinese Academy of Sciences, No. 9 Dengzhuang South Road, Beijing 100094, China; shantc@radi.ac.cn (T.S.); wangcl@radi.ac.cn (C.W.); wqc0722@gmail.com (Q.W.); libin01@radi.ac.cn (B.L.); yubo@radi.ac.cn (B.Y.); xeeshanshirazi@hotmail.com (Z.S.); linzhy@radi.ac.cn (Z.L.); wuwei@radi.ac.cn (W.W.)

<sup>2</sup> University of Chinese Academy of Sciences, Beijing 100049, China

<sup>3</sup> Hainan Key Laboratory of Earth Observation, Institute of Remote Sensing and Digital Earth, Chinese Academy of Sciences, Sanya 572029, China

\* Correspondence: chenfang\_group@radi.ac.cn; Tel.: +86-10-8217-8105

Academic Editors: Ioannis Gitas and Prasad S. Thenkabail

Received: 12 June 2017; Accepted: 12 July 2017; Published: 16 July 2017

**Abstract:** Biomass burning is a worldwide phenomenon, which emits large amounts of carbon into the atmosphere and strongly influences the environment. Burned area is an important parameter in modeling the impacts of biomass burning on the climate and ecosystem. The Medium Resolution Spectral Imager (MERSI) onboard FengYun-3C (FY-3C) has shown great potential for burned area mapping research, but there is still a lack of relevant studies and applications. This paper describes an automated burned area mapping algorithm that was developed using daily MERSI data. The algorithm employs time-series analysis and multi-temporal 1000-m resolution data to obtain seed pixels. To identify the burned pixels automatically, region growing and Support Vector Machine) methods have been used together with 250-m resolution data. The algorithm was tested by applying it in two experimental areas, and the accuracy of the results was evaluated by comparing them to reference burned area maps, which were interpreted manually using Landsat 8 OLI data and the MODIS MCD64A1 burned area product. The results demonstrated that the proposed algorithm was able to improve the burned area mapping accuracy at the two study sites.

**Keywords:** image classification; remote sensing; burned area; FengYun-3C Medium Resolution Spectral Imager (FY-3C MERSI)

---

## 1. Introduction

Biomass burning is a naturally reoccurring worldwide phenomenon. It has environmental and ecological consequences such as effects on the global carbon budget, changes to the global carbon cycle, and disruption of ecosystem succession [1]. The environmental, economic, and social impacts of biomass burning have raised concerns among many policy- and decision-makers and have highlighted the need to manage them. Accurate and actionable information on different aspects of fires is needed for policy- and management-related issues. For example, the spatial and temporal distribution of fires is an important yet basic form of information that requires accurate mapping techniques [2].

Remote sensing technology provides a unique perspective for observing and monitoring fire events [3,4]. In the past few decades, it has been used quite extensively in burned area mapping studies. For local-scale burned area mapping, medium resolution satellite sensors such as the Thematic Mapper (TM) [5–8] and High Resolution Visible (HRV) [9] meet the mapping requirements, and high-resolution sensors such as IKONOS, Quickbird, and Worldview [10,11] have also been

widely used for high-resolution mapping studies. For global and regional burned area mapping, satellite sensors such as the Advanced Very High Resolution Radiometer (AVHRR) [12–14], the Moderate Resolution Imaging Spectroradiometer (MODIS) [15–17], VEGETATION [18,19], and the Medium Resolution Imaging Spectrometer (MERIS) [20] provide low-cost data and have the advantages of large spatial coverage and frequent overpasses. Since Synthetic Aperture Radar (SAR) imagery has the ability to penetrate clouds and fire smoke [21], the integration of optical and SAR data for fire monitoring can reduce the intrinsic limitations in the exclusive use of optical data. An approach has been developed based on fuzzy sets theory and a region-growing algorithm to map burned areas using Landsat TM and (C-band) ENVISAT Advanced Synthetic Aperture Radar (ASAR) images [22].

Currently, various satellite-based burned area products, including GDED4 [23], MCD45A1 [24], L3JRC [25], GLOBSCAR [26], GBA2000 [27], and MCD64A1 [23], have been developed. These burned area mapping algorithms can generally be categorized into two types; the single-scene approach and the multi-temporal analysis approach. The single-scene approach identifies burned and unburned pixels based on their spectral differences in a single post-fire image. For example, a logistic regression model was developed using a single-scene post-fire Landsat TM image [5]; a Classification and Regression Trees (CART) approach using AVHRR data and SPOT-VEGETATION imagery [28,29] has been proposed; the GLOBSCAR global burned area product [30] is created using ATSR-2 and AATSR post-fire imagery in contextual and fixed-threshold algorithms; a Support Vector Machine (SVM) combined with the region-growing method was applied to post-fire MODIS data [31]; and a spatial autocorrelation analysis approach was applied to single MODIS and ASTER scenes [32].

The multi-temporal analysis approach detects burned pixels by analyzing the changes in the spectral information contained in multi-temporal data. For example, the GBA2000 global burned area product was developed using nine different regional algorithms to analyze multi-temporal 1-km VGT daily imagery [19], while a modified GBA-2000 regional algorithm was used to map the global burned area with a temporal index by employing 1-km multi-temporal satellite data. Also, the MCD45A1 burned area product algorithm applies a predictive bi-directional reflectance model to detect burned pixels using multi-temporal MODIS data [24,33]; the MCD64A1 burned area product uses a multi-temporal algorithm to analyze variations in daily MODIS surface reflectance data in order to detect sharp declines in the vegetation index and uses active fires to identify training pixels for the extraction of burned areas [16,34]. A burned area can also be detected by comparing 10-day composites of AVHRR vegetation indices and near-infrared reflectance [35]. Among many others, recent multi-temporal algorithms for burned area mapping include a method that uses Landsat data to compare 40-day composites of the spectral index from four different time periods [36], a semi-automated method for burned area mapping using Normalized Burned Ratio (NBR) MODIS time-series imagery [37], and data fusion between 30-m multi-temporal Landsat ETM+ data and 1000-m MODIS active fire data, which was used to create a burned area map at 30-m resolution.

In most burned area mapping studies, vegetation indices (VIs) are widely used and have proven to be helpful [31]. The use of VIs for burned area mapping can be categorized into three types. The first type of VI, which includes the Normalized Difference Vegetation Index (NDVI), the Global Environmental Monitoring Index (GEMI), and the Soil-Adjusted Vegetation Index (SAVI), is designed to indicate the interruption to photosynthesis caused by fire [38]. The second type of VI, which includes NBR, the Normalized Difference Infrared Index (NDII) [39], and the Short Wave Vegetation Index (SWVI), demonstrates the water loss after the incidence of fire [40]. The third type detects the temperature of the burned area and the increase of surface absorption; this type includes VI3 [41], VI6T [42], and the NIR-SWIR-Thermal index version 1 (NSTv1) [43]. In addition, active fires extracted using thermal anomalies are considered to be an indicator of fire events, and several burned area mapping methods use active fires for training burned pixels in hybrid algorithms [16].

The FengYun-3 (FY-3) satellites are second-generation Chinese polar-orbiting meteorological satellites. The FY-3 series of satellites was developed and manufactured for two objectives; FY-3A and FY-3B for research and development and the other satellites for operational purposes. FY-3A, FY-3B, and FY-3C were launched in 2008, 2010, and 2013 respectively. Several studies have

demonstrated the great potential of FY-3 for fire detection and monitoring. A new model named the Normalized Difference Thermal Index (NDTI), which was developed for fire detection and monitoring, is widely applied to data from the sensors on FY-3 [44]. A new model for fire forecasting based on the fire monitoring database and FY-1, FY-3, and other satellite data has also been developed [45]. A method for monitoring thermally anomalous pixels using Visible and Infra-Red Radiometer (VIRR) data has been proposed and has been validated by biomass burning data [46]. The Medium Resolution Spectral Imager (MERSI) is a key payload onboard all the FY-3 series satellites. MERSI has 20 channels, of which 19 are located in VIR/NIR/SWIR spectral ranges with wavelengths ranging from 0.41 to 2.13  $\mu\text{m}$ , together with one broad band located in the TIR that has a wavelength of 11.25  $\mu\text{m}$ . The VIR and TIR channels have a spatial resolution of 250 m, while the other bands have a resolution of 1000 m. A large number of studies have used MODIS data for burned area mapping. Similarly to MODIS, MERSI also has great potential for detecting burned pixels but lacks recognition among researchers, and, consequently, not many studies use MERSI data. Although the MODIS daily active fire products MOD14A1 and MYD14A1 were used in the proposed method because of their high reliability and availability, FY-3 also has a series active fire product produced using VIRR data. In the future, the FY-3 active fire product will be improved, and it will be possible to use it together with the proposed method. In addition, both Terra and Aqua have exceeded their mission lifetimes (they were launched in 1999 and 2004 respectively); therefore, MERSI and other data could fill the gaps in the imaging of burned areas.

Presently, most of the studies using MERSI data detect burned areas using visual interpretation or empirical thresholds and extraction approaches. For these reasons, an efficient automated algorithm for MERSI-based burned area mapping is urgently needed. In this study, we assessed the ability of the FY-3 MERSI sensor to detect burned pixels (Figure 1). We developed an automated burned area mapping algorithm for multi-temporal FY-3 MERSI data and tested its performance on the Carlton Complex Fire in America and the British Columbia Forest Fire in Canada. A comparison between our results and MODIS burned area products is also presented in this paper.

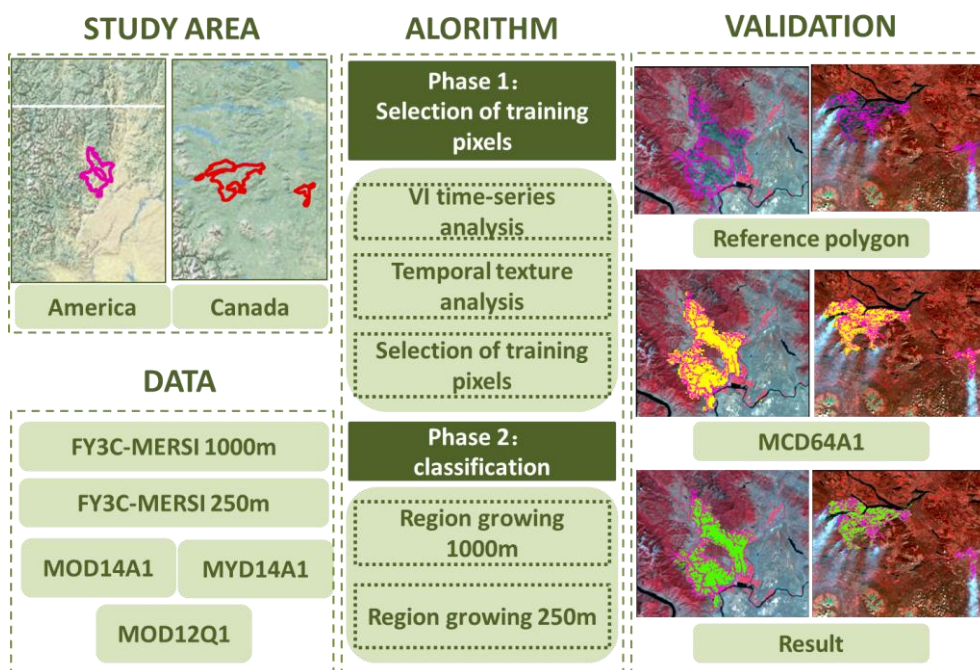
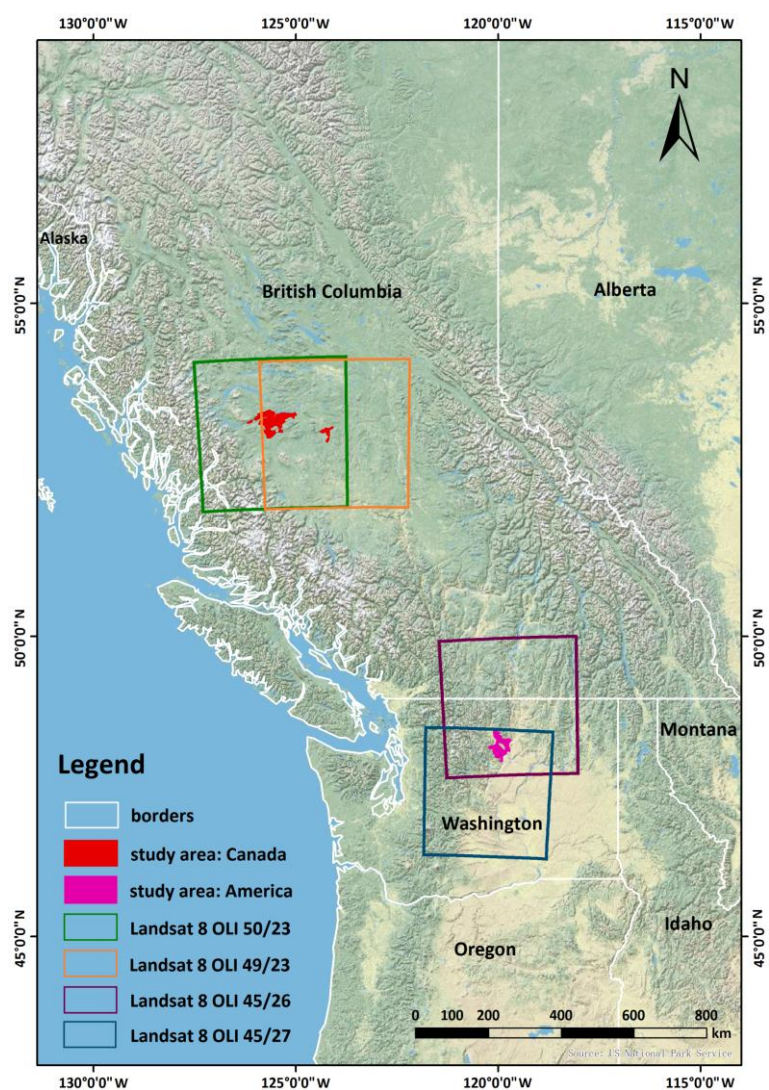


Figure 1. Graphical Abstract.

## 2. Materials and Methods

### 2.1. Study Area

Two large-scale fire events, the Carlton Complex Fire (America) and the British Columbia Forest Fire (Canada), were selected for this study (Figure 2). The Carlton Complex Fire broke out in north-central Washington on 14 July 2014 and lasted for about three weeks. A total of 103,643 ha of forest were burned during the fire (<http://inciweb.nwccg.gov>). The British Columbia forest fire began in British Columbia on 8 July 2014 and lasted for about four weeks. The total size of the burned area was approximately 133,100 ha (<http://bcwildfire.ca>).



**Figure 2.** Two study areas and Landsat 8 OLI datasets acquired for validation.

### 2.2. Data

FY-3C MERSI 1000-m and 250-m datasets were used in this study (Table 1). The MERSI datasets were calibrated to obtain the top of atmosphere (TOA) reflectance using the calibration factors provided at [http://fy3.satellite.cma.gov.cn/PortalSite/Download/FY3C/CalibrationCoefficient/Update%20of%20Calibration%20for%20Reflective%20Solar%20Bands%20of%20MERSI\\_20140618.doc](http://fy3.satellite.cma.gov.cn/PortalSite/Download/FY3C/CalibrationCoefficient/Update%20of%20Calibration%20for%20Reflective%20Solar%20Bands%20of%20MERSI_20140618.doc). The geo-registration of the imagery was based on the GEO files, which are provided as auxiliary data for the MERSI L1 data set and contain the geo-referencing information for each pixel.

**Table 1.** Properties of the Medium Resolution Spectral Imager (MERSI) bands used.

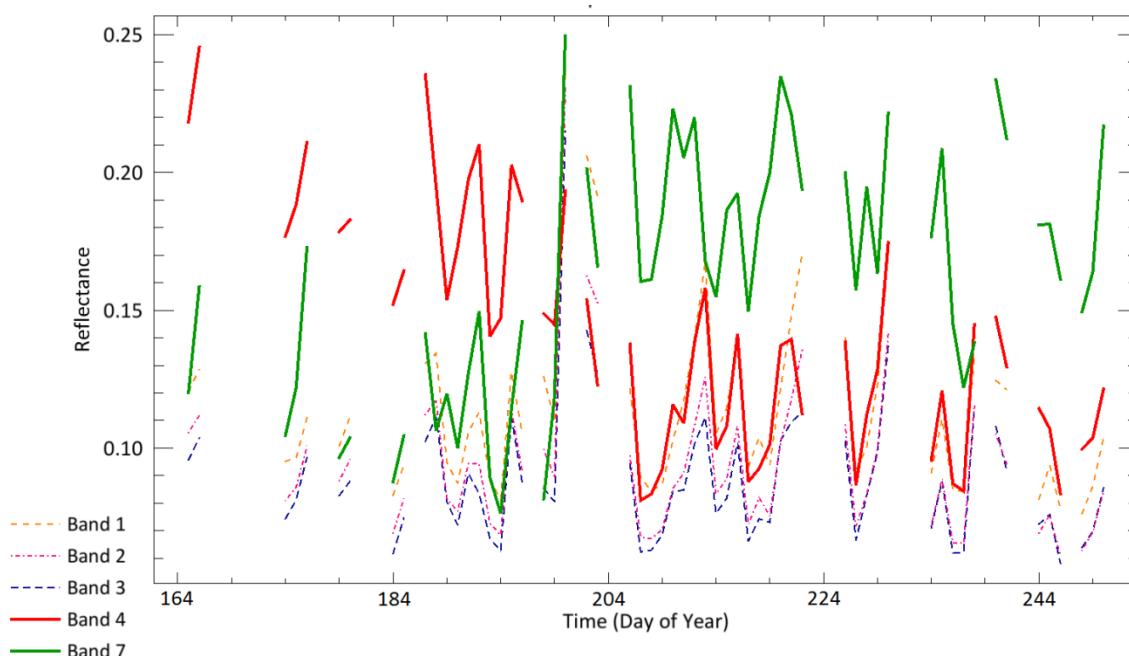
Band	Wavelength ( $\mu\text{m}$ )	SNR <sup>1</sup> or Neq <sup>2</sup> or NEAT <sup>3</sup> @ <sup>4</sup> Specified Input	IFOV <sup>5</sup> @ s.s.p <sup>6</sup> (m)
1	0.465–0.475	100 @ 50% albedo	250/1000
2	0.500–0.700	100 @ 50% albedo	250/1000
3	0.600–0.700	100 @ 50% albedo	250/1000
4	0.815–0.915	100 @ 50% albedo	250/1000
5	8.55–13.55	0.3 K @ 300 K	250/1000
7	2.080–2.180	0.07%	1000

<sup>1</sup> SNR means Signal Noise Ratio. <sup>2</sup> Neq means Noise Equivalent Reflectivity. <sup>3</sup> NEAT means Noise Equivalent Temperature Difference. <sup>4</sup> The symbol (@) means ‘at’. <sup>5</sup> IFOV means Instantaneous Field Of View. <sup>6</sup> s.s.p means Sub Satellite Point.

FY-3 does not offer an operational cloud product so all the clouds in the imagery were masked using empirical thresholds. The condition for cloud mask and smoke is:

$$T(x,y) < 283\text{K}, \quad (1)$$

where  $T(x,y)$  is the brightness temperature of the pixel at the location  $(x,y)$ , which can be obtained by using band 5 data. The threshold of 283 K is set empirically [47]. The brightness temperature of clouds is usually less than 283 K, while that of the ground is higher than 283 K. This is a simple way to remove cloud and smoke. As the time-series analysis algorithm used in this study is robust, a small amount of cloud and smoke will not affect the results. Figure 3 shows the burned area reflectance of the five bands from Table 1 change in the time series data of the Carlton Complex Fire after removing the cloud. The changes of each band in the time series are more obvious, especially band 4 (NIR) and band 7 (SWIR). The reflectance of band 4 drops rapidly around 200, and the reflectance of band 7 has a sharp increase at the same time.

**Figure 3.** The spectral properties of burned areas in the time series data (after removing the cloud).

In addition, the MODIS MOD14A1/MYD14A1 level 3 daily active fire products [15] were used for hot spot identification, and the MODIS MOD12Q1 product was used to obtain land cover information for the study sites [48].

The algorithm is generally divided into two phases (Figure 1): (1) selection of training pixels based on 1000-m resolution MERSI data, which offers more spectral information through the use of more Vis, and (2) classification; first the region growing method is applied to 1000-m MERSI data to calculate the core burned area, and then the same classification method is applied to the 250-m MERSI data set by using the core burned area as a seed to obtain results at a finer spatial resolution. The first phase is mainly based on the methodology proposed by Giglio [16].

### 2.3. Selection of Training Pixels

#### 2.3.1. VI Time-Series Analysis

NDVI, NBR, and VIT were selected as fire-sensitive VIs that could be used for the discrimination of the burned area [43]. FY-3C MERSI-based daily NDVI, NBR, and VIT were calculated as follows (Figure 4: Step 1):

$$NDVI_i = (q_{4,i} - q_{3,i}) / (q_{4,i} + q_{3,i}), \tag{2}$$

$$NBR_i = (q_{4,i} - q_{7,i}) / (q_{4,i} + q_{7,i}), \tag{3}$$

$$VIT_i = (q_{4,i} - q_{5,i} / 1000) / (q_{4,i} + q_{5,i} / 1000), \tag{4}$$

where the daily reflectance is denoted as  $\rho_{b,i}$ ,  $b$  is the MERSI band number, and  $i$  is the observation number in the time series ( $i = 1, 2, 3, \dots, N$ ). The range of time series is about three months; that is, from 11 June 2014 to 11 September 2014 for the Carlton Complex Fire and from 1 June 2014 to 31 August 2014 for the British Columbia forest fire.

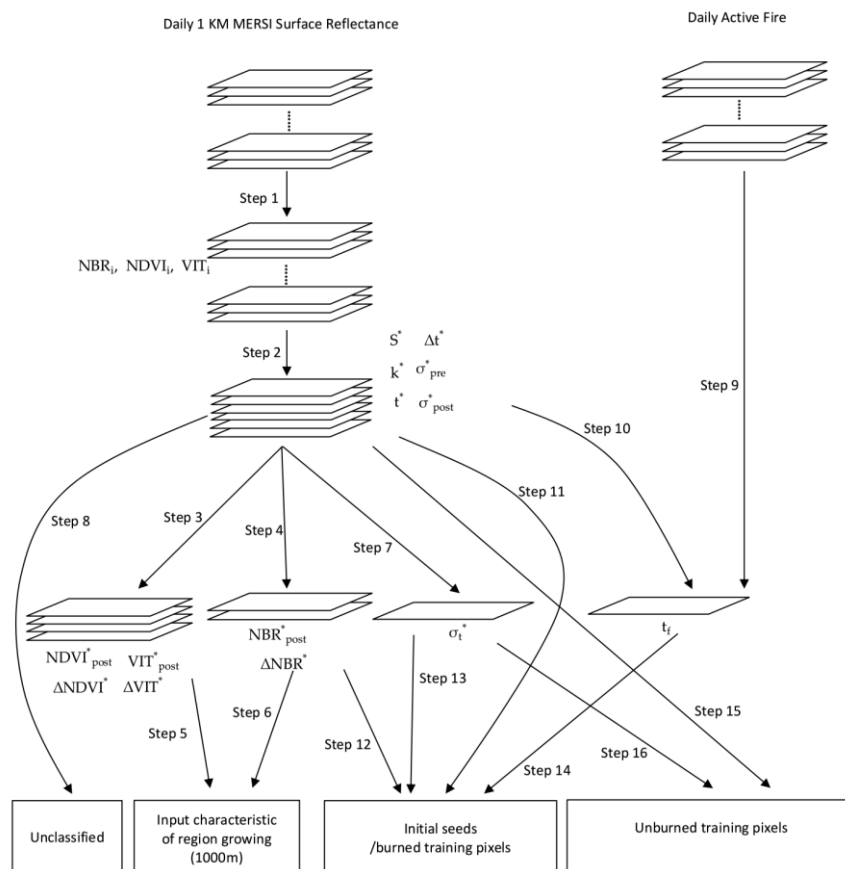


**Figure 4.** Flowchart for the selection of training pixels. There are a total of 16 steps. (1) Analysis of vegetation indices (VIs) time series (steps 1–6) (Section 2.3.1); (2) Temporal texture analysis (steps 6 and 7) (Section 2.3.2); and (3) Selection of training pixels (steps 9–16) (Section 2.3.3).

In burned areas, VIs show notable changes between the pre- and post-fire imagery; therefore time-series analysis was carried out to locate abrupt changes in the VI time series. It is important to note that the values of VIs also fluctuate as a result of other factors such as varying viewing and illumination angles and varying atmospheric conditions. These biases were removed from the time series by using the two adjacent sliding temporal windows approach. Statistics were computed for the  $k$ th pre-fire and post-fire window for all VIs:

$$VI_{pre}(x,y,k) = \text{mean}(VI_i(x,y),p) \quad i \in (k, \dots, k+W-1), \quad (5)$$

$$\sigma_{pre}(x,y,k) = \text{stdev}(VI_i(x,y),p) \quad i \in (k, \dots, k+W-1), \quad (6)$$

$$VI_{post}(x,y,k) = \text{mean}(VI_i(x,y),p) \quad i \in (k+W, \dots, k+2W-1), \quad (7)$$

$$\sigma_{post}(x,y,k) = \text{stdev}(VI_i(x,y),p) \quad i \in (k+W, \dots, k+2W-1), \quad (8)$$

where mean and stdev denote the  $p$ -percent trimmed mean and standard deviation of the pre- and post-fire windows, respectively. As  $p$  was set to 10% for this study, observations above or below 10% were excluded. The setting of  $p$  reduces the impact of potential outliers within a sliding window. However, using a triangular weighting window in Equations (5)–(8) to replace  $p$  could improve the precision of a VIs change, and we may achieve better results.  $(x, y)$  is the location of the 1000-m grid cell within the FY-3C/MERSI tile [16].  $k$  ( $k=1, 2, \dots, N-2W+1$ ) indicates the position of the sliding window within the time series, where  $W$  is the length of the sliding window. To decrease or eliminate disturbing factors and make the separability of the VIs more obvious,  $W$  was set to 10, as in [16].

The separability measurement,  $S$ , was used to identify abrupt changes in the time series [16].  $S$  is defined as:

$$S_{VI}(x,y,k) = \frac{VI_{pre}(x,y,k) - VI_{post}(x,y,k)}{[\sigma_{pre}(x,y,k) + \sigma_{post}(x,y,k)]/2'} \quad (9)$$

if rapid decreases in the VIs occur and  $S_{VI}$  is large and positive, this is indicative of fire events. If the VI values are stable, then  $S_{VI}$  fluctuates around 0 ( $S_{VI} \approx 0$ ). However, if rapid increases in VIs occur, then  $S_{VI}$  will be large and negative.  $\sigma_{pre}$  and  $\sigma_{post}$  are used to prevent large differences between the pre- and post-fire windows that are not due to fire-related events.

The maximum separability  $S^*_{VI}$  of the time series for each pixel was calculated for each VI time series, and the value of  $k$  at which  $S^*_{VI}$  occurs is designated as  $k^*_{VI}(x, y)$ . The date corresponding to the maximum change was designated as  $t^*_{VI}(x, y)$ , which is the midpoint of the interval between the  $k^*_{VI}$  pre- and post-fire windows and was defined as:

$$t^*_{vi}(x,y) = [t(x,y,k^*_{vi} + W - 1) + t(x,y,k^*_{vi} + W)]/2. \quad (10)$$

The length of the interval was also calculated and was defined as:

$$\Delta t^*_{vi}(x,y) = t(x,y,k^*_{vi} + W - 1) - t(x,y,k^*_{vi} + W). \quad (11)$$

In most cases, the maximum changes in the VIs (NDVI, NBR, and VIT) occurred at approximately the same time. In order to reduce the computation time, the NBR was, therefore, used to calculate  $S^*$ ,  $k^*$ , and  $t^*$ , meaning that  $S^* = S^*_{NBR}$ ,  $k^* = k^*_{NBR}$ ,  $t^*(x, y) = t^*_{NBR}(x, y)$ , and  $\Delta t^*(x, y) = \Delta t^*_{NBR}(x, y)$  (Figure 4, Step 2). The trimmed standard deviations of the pre- and post-fire windows associated with  $k^*$  for each pixel were calculated and denoted as  $\sigma^*_{pre}$  and  $\sigma^*_{post}$ , respectively; these were subsequently used to measure the geo-location error of the MERSI data.

The composite VI images could be then calculated by using  $k^*$  with the VI time series:

$$VI^*_{post}(x,y) = VI_{post}(x,y,k^*), \quad (12)$$

$$\Delta VI^*(x,y) = VI^*_{pre}(x,y) - VI^*_{post}(x,y). \quad (13)$$

The composite NDVI, NBR, and VIT images were calculated using the above equations by substituting the values of  $NDVI^*_{pre}$ ,  $NDVI^*_{post}$ ,  $\Delta NDVI^*$ ,  $NBR^*_{pre}$ ,  $NBR^*_{post}$ ,  $\Delta NBR^*$ ,  $VIT^*_{pre}$ ,

$VIT_{\text{post}}^*$ , and  $\Delta VIT^*$  (Figure 4, Steps 3 and 4). These composite images were used as input characteristics for the region growing in described in Section 2.4. (Figure 4, Steps 5 and 6).

### 2.3.2. Temporal Texture Analysis

The maximum changes in the time series of burned pixels are caused by fire, and, thus, the day of maximum change ( $t^*$ ) can be taken as the day of the fire event; adjacent burned pixels should also have a similar  $t^*$ . Burned areas should, therefore, have a more consistent value of  $t^*$  and also be more spatially clustered than unburned pixels. The local standard deviation of  $t^*$  within rook's-case windows was calculated to describe the spatial coherence of the burned areas. This standard deviation map was filtered using an edge-restoring filter that selected the 33rd percentile pixels within queen's-case windows to prevent any loss of the edge pixels of the burn scar. (Selecting the 50th percentile instead would be the equivalent of a median filter.) The results were denoted as  $\sigma_t^*$  (Figure 4, Step 7). The rook's windows considered the neighborhood of four pixels adjacent to each pixel, while the queen's windows considered a neighborhood of eight pixels [49,50]. Note that the unit of measurement for both  $t^*$  and  $\sigma_t^*$  is 'day'.

There are always invalid observations in the VI time series due to cloud obscuration or other reasons; for a fixed number of observations ( $W$ ), the length of time between the pre- and post-fire windows was, therefore, of variable length. To estimate the uncertainty in the results,  $\Delta t^*(x, y)$  was used to describe the gap between the earliest date in the post-fire window and the latest date in the pre-fire window.

One of the factors that causes variations in VI time series, other than fire events, is the geo-location error in MERSI data. The magnitude of the shift between two images is about one to two pixels. As a result of this geo-location error, the VI values for one pixel will likely incorporate values from neighboring pixels. While the daily variations in the optical factors were smoothed by using the moving average described in the previous step, the variations caused by the geo-location error could not be removed as easily. Also, for homogeneous areas such as the core burned area region, the pixels have similar VI values and the shift between images will not strongly affect the time series, which will, therefore, be less sensitive to the geo-location error. Due to the geo-location error, burned pixels and unburned pixels will likely be mixed in the heterogeneous areas such as pixels near to or within the transition zones between burned and unburned areas. This does cause large fluctuations in the time series. Therefore, significant decreases in Vis may be caused by shifts in imagery rather than fire.

As heterogeneous areas are more sensitive to geo-location errors, the heterogeneous area pixels were not processed until the second phase. In the second phase, these unclassified pixels would be classified again using an SVM classifier and the region growing method using 250-m imagery. The pixels at location  $(x, y)$  were treated as pixels from homogeneous areas and were retained if the following conditions were satisfied; any pixels that did not satisfy these criteria were marked as unclassified (Figure 4, Step 8):

$$\sigma_{\text{pre}}^*(x, y) \leq 0.2, \quad (14)$$

$$\sigma_{\text{post}}^*(x, y) \geq 0.2, \quad (15)$$

These criteria, which are conservation thresholds used to identify heterogeneous areas with low VIs and small differences between pre- and post-fire windows, were selected empirically.

### 2.3.3. Selection of Training Pixels

This section discusses two groups of criteria. The objective of the first group of criteria is to detect burned training pixels. The cumulative active fire map, abbreviated as  $t_f(x, y)$ , was developed using the MOD14A1/MYD14A1 active fire product, which was re-projected to match the MERSI data (Figure 4, Step 9). The magnitude of the re-projection error caused by geo-location was about one to two pixels and was reduced by applying the steps described below. The cumulative active fire map basically matched the dates of the fire detected by the MODIS products during the time period being investigated at a location  $(x, y)$ ,  $(t_f(x, y))$ . If multiple fires were detected within the same pixel on

different dates, the date nearest to  $t^*(x, y)$  was chosen to be  $t_f(x, y)$  (Figure 4, Step 10). The cumulative fire data was used to select the burned area as training pixels (burned training pixels). Since the selection of training pixels was based on 1000-m imagery, some areas at the edges of a cluster of active fire pixels may be unburned. To make sure that all the training pixels were actually burned, those pixels which were less likely to be detected as burned area had to be removed by morphological erosion using a  $3 \times 3$  structuring element. The pixels at location  $(x, y)$  that satisfied the following conditions were selected as burned training pixels (Figure 4, Steps 11–14).

$$S_{VI}^*(x, y) \geq 2, \quad (16)$$

$$\sigma_t^*(x, y) \leq 1 \text{ days}, \quad (17)$$

$$NBR_{\text{post}}^*(x, y) < 0, \quad (18)$$

$$\Delta NBR^*(x, y) > 0.2, \quad (19)$$

$$|t_f(x, y) - t^*(x, y)| \leq \Delta t^*(x, y), \quad (20)$$

Equations (16) and (17) ensure high VI series separability and high temporal–spatial homogeneity. The approximate date of the burned training pixels, i.e., the date on which the maximum separability of the VI series occurs ( $t^*(x, y)$ ), should be close to the date on which the active fire was detected ( $t_f(x, y)$ ), which is restricted by Equation (20).

The objective of the second group of criteria is to detect unburned training pixels. If the conservative thresholds are developed empirically as follows, the two criteria given below can be used to identify pixels that have low temporal–spatial homogeneity and very low VI separability ( $S_{VI}$ ).

$$S_{VI}^*(x, y) < 2, \quad (21)$$

$$\sigma_t^*(x, y) > 8 \text{ days}, \quad (22)$$

The time series for pixels at location  $(x, y)$  that satisfy Equation (21) and (22) without abrupt changes will be stable and have low temporal–spatial homogeneity. These two characteristics were selected empirically [17]. This means that these pixels were unlikely to be burned during the time period being investigated. To further reduce the potential impact of fire, a distance threshold was added:

$$R_d(x, y) > D, \quad (23)$$

where  $R_d(x, y)$  denotes the distance from the pixel at location  $(x, y)$  to the nearest burned training pixel.  $D$  was established empirically and set equal to 3 km [16]. If Equations (21)–(23) were satisfied at the same time, the pixel at location  $(x, y)$  was selected as an unburned training pixel (Figure 4, Steps 15 and 16). [23] limits the distance from unburned training pixels to burned training pixels in order to make sure that none of the unburned training pixels are affected by the fire.

## 2.4. Classification

### 2.4.1. Classification by SVM Classifier

The classification of the burned pixels (Figure 5) was based on the region-growing method. Seed pixels were used in subsequent iterations to classify surrounding pixels as burned or unburned using a queen's-case window. During the first iteration, burned training pixels were selected as seeds. An SVM classifier was trained by the seeds identified at the beginning of classification or in the previous iteration and then used to classify the neighborhood pixels as burned or unburned in each iteration.

If a new burned pixel was detected, it was used as a new seed in the following iteration. The iteration cycle stopped when the number of newly detected burned pixels was 0.

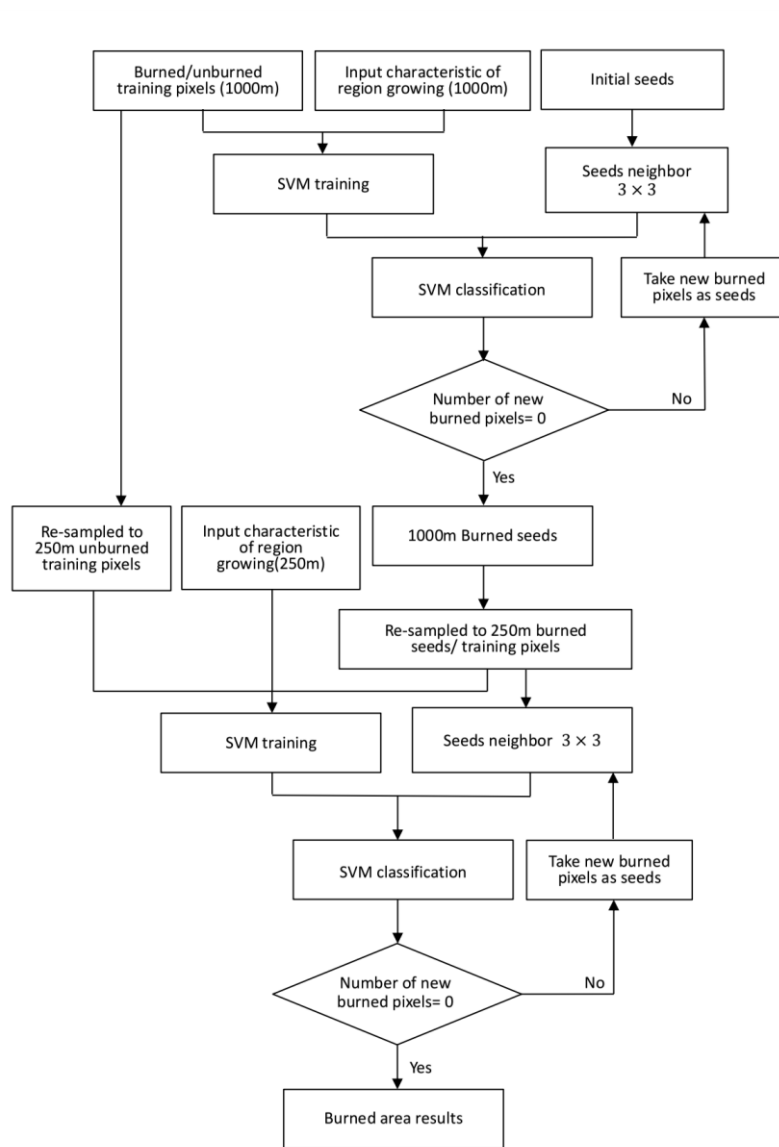


**Figure 5.** Flowchart for the classification of the burned pixels.

The classification was first conducted on the 1000-m VI composite imagery, namely  $NDVI_{post}^*$ ,  $\Delta NDVI^*$ ,  $NBR_{post}^*$ ,  $\Delta NBR^*$ ,  $VIT_{post}^*$  and  $\Delta VIT^*$ . To improve the performance of the method, all the pixels selected as seeds using the 1000-m resolution results were then re-sampled to 250 m resolution and taken as new seeds for burned pixel classification using the 250-m imagery. This is because the spectral information with a resolution of 250 m could be used to improve the accuracy of the method in regions with low fire severity, which are characterized by great spatial heterogeneity or are located at the edge of the fire scar. Individual 250-m MERSI images were selected for analysis within the 1000-m time series. The selection of the imagery from the time series was based on the availability of cloud-free, usable imagery.

The seeds for the 250-m image were generated from the whole 1000-m time series. The dates of these seeds were earlier than the date of the 250-m image to ensure that all the burned pixels identified in the previous analysis had been included. This was achieved by applying the following condition:

$$t_{post}^*(x,y) < t_d \quad (24)$$

where  $t_{\text{post}}^*(x,y)$  is the day after the date of  $S^*$  at location  $(x,y)$  and  $t_a$  is the date of the selected MERSI image. As the NDVI values for images acquired at different seasons have distinct ranges, the re-sampled burned pixels were reevaluated as burned or unburned pixels using a NDVI threshold defined as follows:

$$a \leq \text{NDVI}(x,y) \leq b, \quad (25)$$

The thresholds were determined empirically. Any seed that did not satisfy the above NDVI threshold was discarded. The NDVI value of the seed at  $(x,y)$  was denoted as  $\text{NDVI}(x,y)$ .  $a$  and  $b$  are the 10th percentile and 60th percentile, respectively, of the NDVI values of all the seeds.

#### 2.4.2. Use of Vegetation Indexes in the SVM Classifier

A total of five vegetation indices were calculated to be used as the input data for the SVM classifier. Even though not all of these indices are fire sensitive, we used all five indices to provide as much information as possible. The NDVI (Equation (2)), VIT (Equation (4)), NDWI [51], BAI [52], and EVI [53] for the chosen imagery were calculated, where:

$$\text{NDWI}_i = (Q_{2,i} - Q_{4,i}) / (Q_{2,i} + Q_{4,i}), \quad (26)$$

$$\text{BAI}_i = 1 / \left( (0.1 + Q_{3,i})^2 + (0.06 + Q_{4,i})^2 \right), \quad (27)$$

$$\text{EVI}_i = 2.5 (Q_{4,i} - Q_{3,i}) / (Q_{4,i} - 6Q_{3,i} - 7.5Q_{1,i} + 1). \quad (28)$$

In order to eliminate false burned pixels during classification, only the pixels with the lowest 70% of band 4 values were labeled as burned.

### 3. Results

Figures 6 and 7 show the results of applying the proposed algorithm at the two study sites, respectively. The reference polygons were derived by interpreting the 30-m Landsat-8 OLI imagery (Figure 2), which is shown as a false color composite mosaic (R-G-B: 5-4-3), acquired on the same day as the 250-m MERSI data. The MCD64A1 burned area product was used to compare the results with those obtained using the proposed algorithm. Magnified subfigures showing differences in the results are also shown in Figures 6 and 7. It can be seen that our results show finer spatial detail than MODIS MCD64A1. The result of the proposed algorithm is more likely to be smaller than the reference polygons, while the result of MODIS MCD64A1 is more likely beyond the reference polygons.

An accuracy assessment for the two study sites is shown in Table 2. The results obtained using the proposed algorithm have a higher kappa coefficient, indicating that the proposed algorithm is more accurate in the study region. However, the proposed algorithm has a higher omission error because some small burned areas were missed using this algorithm.

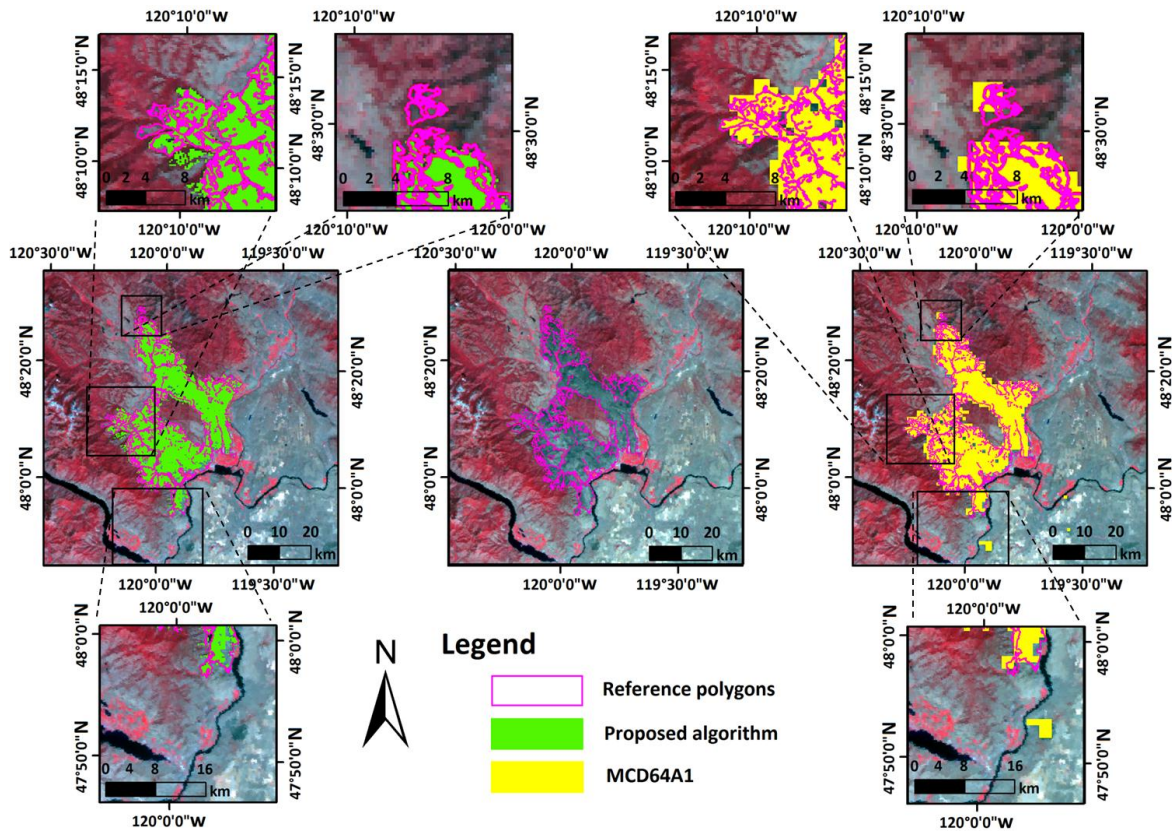


Figure 6. Comparison of burned area results obtained using different methods (study area: America).

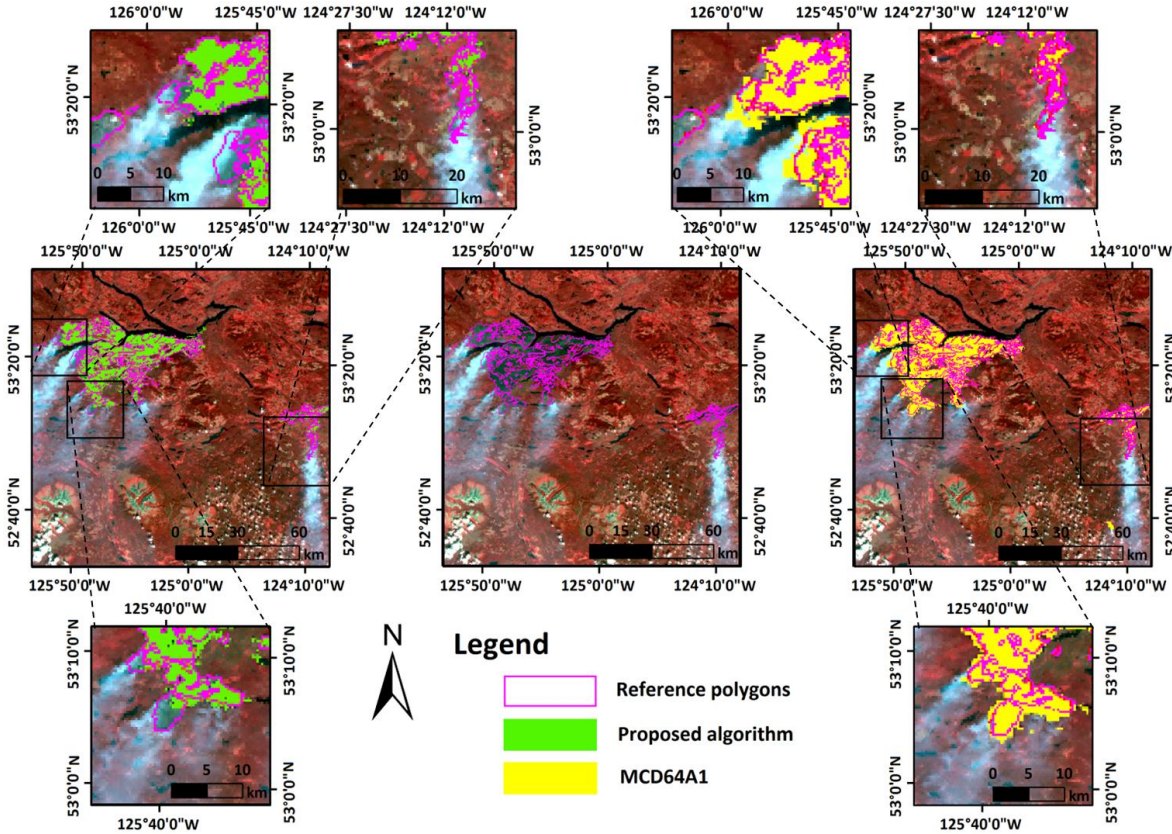


Figure 7. Comparison of burned area results obtained using different methods (study area: Canada).

**Table 2.** Comparison of the accuracy of the proposed algorithm and MODIS MCD64A1 for the two study sites.

Study Area	Proposed Algorithm			MODIS MCD64A1		
	OE (%)	CE (%)	Kappa	OE (%)	CE (%)	Kappa
America	11.32	14.77	0.8680	6.67	20.58	0.8567
Canada	17.21	23.94	0.7914	16.44	31.00	0.6893

#### 4. Discussion

The results obtained suggest that the algorithm using the 250-m resolution input data makes a better distinction between burned pixels and unburned pixels compared to the MODIS burned area product, which uses 1000-m resolution data as input data. To some extent, using 250-m resolution data in the proposed algorithm can explain the better kappa coefficient and the lower commission error obtained for both study areas. The region-growing method used in the algorithm reduces the omission error, but the omission error is higher compared to the MCD64A1 product at both study sites. The omission errors are a consequence of the missed seeds; i.e., if a seed is not selected for an isolated burned area, it will not be translated into burned area by the region-growing method, and this results in an omission error. As MERSI data suffer from a geo-location problem, pixels that are less likely to be detected as burned area need to be removed by morphological erosion using a  $3 \times 3$  structuring element. As the erosion mask eliminates all clusters smaller than  $3 \times 3$  km, morphological erosion can remove small clusters of burned areas. This is a key cause of omission errors. If the geo-location of MERSI data could be improved, morphological erosion could be omitted in future studies. The burned area mapping results should then retain more small burned areas, and the omission error would be reduced. In addition, the proposed method is applicable to large wildfires, but that could be expected to a certain level due to the low pixel resolution. In this case, the employment of additional burn scars should be considered in future studies in order to make this approach worth using.

Cloud obstruction can also lead to omission errors and is an inherent limitation of single-scene algorithms. The proposed method uses a single-scene algorithm for burned area mapping because geo-location errors exist in MERSI data, which makes accurate mapping of burned area using multi-temporal algorithms very difficult. However, single-scene algorithms have been shown to be affected by cloud obscuration. To overcome this problem, the geo-location accuracy of 250-m MERSI data needs first to be determined so that a multi-temporal algorithm can then be used instead. The suitability of the proposed algorithm for different regions at a global scale with various vegetation types still needs to be tested and established.

To deal with the geo-referencing problem, the homogeneous areas were collected and processed first, with the heterogeneous areas being processed subsequently. This procedure is useful only if the wildfire burns all the vegetation in a homogeneous way, as was the case in the two study areas that we chose. As pixels with a size of  $1 \times 1$  km were used for the burned area mapping in this paper, this underlying assumption may be difficult to meet in many ecosystems such as South American dry forests, Chaparral, or the Mediterranean basin. The diverse conditions encountered in different ecosystems should be considered when attempting to apply the proposed method in future studies.

The sound performance of the proposed algorithm can be attributed to the following reasons. (1) A better spatial resolution (250 m) could help to increase the performance of MERSI data. (2) Multiple vegetation indices provide more sufficient information for guiding the selection of training pixels, which are used in the supervised classification of burned areas. (3) An SVM classifier combined with region growing is suitable for the capability of FY3C MERSI data.

#### 5. Conclusions

In this article, an automated burned area mapping algorithm was proposed based on FY-3C MERSI data. Time-series analysis and active fire products were used to guide the seed selection, and an SVM combined with the region-growing method was used to distinguish between the burned and

unburned pixels. An evaluation of the performance of the algorithm was carried out at two study sites. The accuracy assessment and validation were made by comparing our results with the MODIS MCD64A1 burned area product and reference results derived from Landsat OLI data. The results were found to be accurate.

A comparison between the results of applying the proposed algorithm and the existing algorithm to burned area mapping leads to the following conclusions.

1. The selection of initial burned seeds is similar to the method proposed by Giglio [16], especially in terms of the definition of the separability of the VIs. One difference between the two methods is that we proposed the use of more than one VI as a burned area feature, based on the characteristics of MERSI data. The other main difference is that between the region-growing methods used in the two papers. The method we proposed used an SVM and the region-growing method simultaneously. These could make the method more suitable for burned area mapping using MERSI data.
2. Regarding the selection of a burned area index for FY-3C MERSI, we analyzed time series of different indices and performed a quantitative analysis of these indices in the burned and unburned areas. We then selected several features that were appropriate for use with FY-3C MERSI data in subsequent analysis.
3. Regarding the extraction of a burned area using the SVM and the region-growing method, SVM and region growing are common image classification and image segmentation algorithms. The combination of these two methods makes regional growth criterion more flexible and can produce more accurate burned area mapping results.
4. The algorithm used a combination of multi-temporal data and single-scenes. First we used 1 km multi-temporal data to extract the characteristic parameters and to obtain preliminary burned area classification results. We then used individual scenes from the time series of 250-m resolution MERSI data and carried out the classification again, thereby reducing the influence of the MERSI geo-location errors and producing more accurate burned area mapping results.
5. MERSI data have shown great potential for filling the gaps in the imaging of burned areas of the Earth's surface. Some MODIS products were used in the proposed method like the daily active fire product MOD14A1/MYD14A1 and the land cover product MOD12Q1 because of their high reliability and ready availability. In addition to MOD12Q1, many other land cover products or vegetation indices can be used to extract vegetation regions. FY-3 also produces series of active fire products derived from VIRR data. In the future, it should be possible to use an improved FY-3 active fire product with the proposed method. As both the Terra and Aqua satellites have exceeded their mission lifetimes, it may then be possible to use MERSI and other data to fill the gaps in the imaging of burned areas.

**Acknowledgments:** This research was supported by the International Partnership Program of the Chinese Academy of Sciences (131C11KYSB20160061), the National Natural Science Foundation Project's 'Constructions detection and damage evaluation model after earthquake based on multi-task transfer learning' (41601451) and the International Partnership Program of the Chinese Academy of Sciences (131551KYSB20160002)

**Author Contributions:** Tianchan Shan, Changlin Wang, Fang Chen and Qinchun Wu conceived and designed the experiments; Tianchan Shan and Qinchun Wu performed the experiments; Tianchan Shan, Bin Li and Bo Yu analyzed the data; Zeeshan Shirazi, Zhengyang Lin and Wei Wu contributed analysis tools; Tianchan Shan, Changlin Wang, Fang Chen and Qinchun Wu wrote the paper.

**Conflicts of Interest:** The authors declare no conflict of interest.

## References

1. Crutzen, P.J.; Andreae, M.O. Biomass burning in the tropics: Impact on atmospheric chemistry and biogeochemical cycles. *Science* **1991**, *250*, 1669–1678.
2. French, N.H.F.; Goovaerts, P.; Kasischke, E.S. Uncertainty in estimating carbon emissions from boreal forest fires. *J. Geophys. Res. Atmos.* **2004**, *109*, 646–650.
3. Seiler, W.; Crutzen, P.J. Estimates of gross and net fluxes of carbon between the biosphere and the

- atmosphere from biomass burning. *Clim. Chang.* **1980**, *2*, 207–247.
4. Corona, P.; Lamonaca, A.; Chirici, G. Remote sensing support for post fire forest management. *iForest Biogeosc. For.* **2008**, *1*, 6–12.
  5. Koutsias, N.; Karteris, M. Burned area mapping using logistic regression modeling of a single post-fire landsat-5 thematic mapper image. *Int. J. Remote Sens.* **2000**, *21*, 673–687.
  6. Smith, A.M.S.; Drake, N.A.; Wooster, M.J.; Hudak, A.T.; Holden, Z.A.; Gibbons, C.J. Production of landsat ETM+ reference imagery of burned areas within southern african savannahs: Comparison of methods and application to MODIS. *Int. J. Remote Sens.* **2007**, *28*, 2753–2775.
  7. Stroppiana, D.; Bordogna, G.; Carrara, P.; Boschetti, M.; Boschetti, L.; Brivio, P.A. A method for extracting burned areas from landsat TM/ETM+ images by soft aggregation of multiple spectral indices and a region growing algorithm. *ISPRS J. Photogramm. Remote Sens.* **2012**, *69*, 88–102.
  8. Koutsias, N.; Pleniou, M.; Mallinis, G.; Nioti, F.; Sifakis, N.I. A rule-based semi-automatic method to map burned areas: Exploring the usgs historical landsat archives to reconstruct recent fire history. *Int. J. Remote Sens.* **2013**, *34*, 7049–7068.
  9. Polychronaki, A.; Gitas, I.Z. Burned area mapping in greece using SPOT-4 HRVIR images and object-based image analysis. *Remote Sens.* **2012**, *78*, 424–438.
  10. Garrity, S.R.; Allen, C.D.; Brumby, S.P.; Gangodagamage, C.; Mcdowell, N.G.; Cai, D.M. Quantifying tree mortality in a mixed species woodland using multitemporal high spatial resolution satellite imagery. *Remote Sens. Environ.* **2013**, *129*, 54–65.
  11. Dragozi, E.; Gitas, I.; Stavrakoudis, D.; Theocharis, J. Burned area mapping using support vector machines and the fuzcoc feature selection method on VHR ikonos imagery. *Remote Sens.* **2014**, *6*, 12005–12036.
  12. Jr, D.R.C.; Stocks, B.J.; Levine, J.S.; Cofer, W.R., III; Pierson, J.M. Satellite analysis of the severe 1987 forest fires in northern china and southeastern siberia. *J. Geophys. Res. Atmos.* **1994**, *99*, 18627–18638.
  13. Fraser, R.H.; Li, Z.; Cihlar, J. Hotspot and NDVI differencing synergy (hands): A new technique for burned area mapping over boreal forest. *Remote Sens. Environ.* **2000**, *74*, 362–376.
  14. Gitas, I.Z.; Mitri, G.H.; Ventura, G. Object-based image classification for burned area mapping of creus cape, spain, using NOAA-AVHRR imagery. *Remote Sens. Environ.* **2004**, *92*, 409–413.
  15. Roy, D.; Desclotres, J.; Alleaume, S. The MODIS fire products. *Remote Sens. Environ.* **2002**, *83*, 244–262.
  16. Giglio, L.; Loboda, T.; Roy, D.P.; Quayle, B.; Justice, C.O. An active-fire based burned area mapping algorithm for the MODIS sensor. *Remote Sens. Environ.* **2009**, *113*, 408–420.
  17. Ruiz, J.A.M.; Lázaro, J.R.G.; Cano, I.D.Á.; Leal, P.H. Burned area mapping in the north american boreal forest using terra-MODIS LTDR (2001–2011): A comparison with the MCD45A1, MCD64A1 and BA GEOLAND-2 products. *Remote Sens.* **2014**, *6*, 815–840.
  18. Silva, J.M.N.; Pereira, J.M.C.; Cabral, A.I.; Sá, A.C.L.; Vasconcelos, M.J.P.; Mota, B.; Grégoire, J.M. An estimate of the area burned in southern africa during the 2000 dry season using spot-vegetation satellite data. *J. Geophys. Res. Atmos.* **2003**, *108*, 4498.
  19. Tansey, K.; Grégoire, J.M.; Stroppiana, D.; Sousa, A.; Silva, J.; Pereira, J.M.C.; Boschetti, L.; Maggi, M.; Brivio, P.A.; Fraser, R.; et al. Vegetation burning in the year 2000: Global burned area estimates from spot vegetation data. *J. Geophys. Res. Atmos.* **2004**, *109*, 449–464.
  20. Alonso-Canas, I.; Chuvieco, E. Global burned area mapping from ENVISAT-MERIS and MODIS active fire data. *Remote Sens. Environ.* **2015**, *163*, 140–152.
  21. Hoekman, D.H.; Vissers, M.A.M.; Wielaard, N. Palsar wide-area mapping of borneo: Methodology and map validation. *IEEE J. Sel. Top. Appl. Earth Obs. Remote Sens.* **2010**, *3*, 605–617.
  22. Stroppiana, D.; Azar, R.; Calò, F.; Pepe, A.; Imperatore, P.; Boschetti, M.; Silva, J.M.N.; Brivio, P.A.; Lanari, R. Integration of optical and sar data for burned area mapping in mediterranean regions. *Remote Sens.* **2015**, *7*, 1320–1345.
  23. Giglio, L.; Randerson, J.T.; Van, D.W., G; Collatz, G.J.; Kasibhatla, P.S.; Morton, D.; Defries, R.S. The Global Fire Emissions Database (GFED4) Burned Area Data Set; In proceedings of AGU Fall Meeting, San Francisco, America, 3-7 December, 2012.
  24. Roy, D.P.; Lewis, P.E.; Justice, C.O. Burned area mapping using multi-temporal moderate spatial resolution data—A bi-directional reflectance model-based expectation approach. *Remote Sens. Environ.* **2002**, *83*, 263–286.
  25. Tansey, K.; Beston, J.; Hoscilo, A.; Page, S.E.; Hernández, C.U.P. Relationship between MODIS fire hot spot count and burned area in a degraded tropical peat swamp forest in central Kalimantan, Indonesia. *J.*

- Geophys. Res. Atmos.* **2008**, *113*, 2036–2044.
26. Eva, H.; Lambin, E.F. Burnt area mapping in central africa using ATSR data. *Int. J. Remote Sens.* **1998**, *19*, 3473–3497.
  27. Grégoire, J.-M.; Tansey, K.; Silva, J.M.N. The gba2000 initiative: Developing a global burnt area database from spot-vegetation imagery. *Int. J. Remote Sens.* **2003**, *24*, 1369–1376.
  28. Pereira, J.M.C.; Vasconcelos, M.J.P.; Sousa, A.M. *A Rule-Based System for Burned Area Mapping in Temperate and Tropical Regions Using NOAA/AVHRR Imagery*; Springer Netherlands, 2000; pp. 215–232.
  29. Stroppiana, D.; Tansey, K.; Gregoire, J.M.; Pereira, J.M.C. An algorithm for mapping burnt areas in australia using spot-vegetation data. *IEEE Trans. Geosci. Remote Sens.* **2003**, *41*, 907–909.
  30. Simon, M.; Plummer, S.; Fierens, F.; Hoelzemann, J.J.; Arino, O. Burnt area detection at global scale using ATSR-2: The globscar products and their qualification. *J. Geophys. Res. Atmos.* **2004**, *109*, 2890–2898.
  31. Cao, X.; Chen, J.; Matsushita, B.; Imura, H.; Wang, L. An automatic method for burn scar mapping using support vector machines. *Int. J. Remote Sens.* **2009**, *30*, 577–594.
  32. Lanorte, A.; Danese, M.; Lasaponara, R.; Murgante, B. Multiscale mapping of burn area and severity using multisensor satellite data and spatial autocorrelation analysis. *Int. J. Appl. Earth Obs. Geoinf.* **2013**, *20*, 42–51.
  33. Roy, D.P.; Jin, Y.; Lewis, P.E.; Justice, C.O. Prototyping a global algorithm for systematic fire-affected area mapping using MODIS time series data. *Remote Sens. Environ.* **2005**, *97*, 137–162.
  34. Giglio, L.; Werf, G.R.V.D.; Randerson, J.T.; Collatz, G.J. Global estimation of burned area using MODIS active fire observations. *Chem. Phys.* **2014**, *6*, 957–974.
  35. Chuvieco, E.; Englefield, P.; Trishchenko, A.P.; Luo, Y. Generation of long time series of burn area maps of the boreal forest from NOAA–AVHRR composite data. *Remote Sens. Environ.* **2008**, *112*, 2381–2396.
  36. Toukiloglou, P.; Gitas, I.Z.; Katagis, T. An automated two-step NDVI-based method for the production of low-cost historical burned area map records over large areas. *Int. J. Remote Sens.* **2014**, *35*, 2713–2730.
  37. Hardtke, L.A.; Blanco, P.D.; Valle, H.F.D.; Metternicht, G.I.; Sione, W.F. Semi-automated mapping of burned areas in semi-arid ecosystems using MODIS time-series imagery. *Int. J. Appl. Earth Obs. Geoinf.* **2015**, *38*, 25–35.
  38. Huete, A.R. A soil-adjusted vegetation index (SAVI). *Remote Sens. Environ.* **1988**, *25*, 295–309.
  39. García, M.; Chuvieco, E. Assessment of the potential of SAC-C/MMRS imagery for mapping burned areas in spain. *Remote Sens. Environ.* **2004**, *92*, 414–423.
  40. Fraser, R.H.; Li, Z.; Landry, R. Spot vegetation for characterizing boreal forest fires. *Int. J. Remote Sens.* **2000**, *21*, 3525–3532.
  41. Kaufman, Y.J.; Remer, L.A. Detection of forests using mid-IR reflectance: An application for aerosol studies. *IEEE Trans. Geosci. Remote Sens.* **1994**, *32*, 672–683.
  42. Holden, Z.A.; Smith, A.M.S.; Morgan, P.; Rollins, M.G.; Gessler, P.E. Evaluation of novel thermally enhanced spectral indices for mapping fire perimeters and comparisons with fire atlas data. *Int. J. Remote Sens.* **2005**, *26*, 4801–4808.
  43. Veraverbeke, S.; Harris, S.; Hook, S. Evaluating spectral indices for burned area discrimination using MODIS/ASTER (MASTER) airborne simulator data. *Remote Sens. Environ.* **2011**, *115*, 2702–2709.
  44. Zhao, W.H.; Shan, H.; Zhong, R.X. The normalized difference thermal index (NDTI) for the modis fire detection. *Remote Sens. Technol. Appl.* **2007**, *22*, 403–409.
  45. Wu, S.; Liu, C. A New Model for Fire Forecast, In *Proceedings of Earth Resources and Environmental Remote Sensing/GIS Applications*, Toulouse, France, 20 September 2010.
  46. Wang, Z. Research and evaluation of the algorithm of land surface fire detection based on FY3-VIRR data. *Fire Saf. Sci.* **2011**, *20*, 140–145.
  47. Bastarrika, A.; Alvarado, M.; Artano, K.; Martinez, M.; Mesanza, A.; Torre, L.; Ramo, R.; Chuvieco, E. Bams: A tool for supervised burned area mapping using landsat data. *Remote Sens.* **2014**, *6*, 12360–12380.
  48. Friedl, M.A.; Mciver, D.K.; Hodges, J.C.F.; Zhang, X.Y.; Muchoney, D.; Strahler, A.H.; Woodcock, C.E.; Gopal, S.; Schneider, A.; Cooper, A.; et al. Global land cover mapping from modis: Algorithms and early results. *Remote Sens. Environ.* **2002**, *83*, 287–302.
  49. Overmars, K.P.; Koning, G.H.J.D.; Veldkamp, A. Spatial autocorrelation in multi-scale land use models. *Ecol. Model.* **2003**, *164*, 257–270.
  50. Manish, M. Autocorrelation simulation studies for horizontal transmission of ethno- medicinal-knowledge related with two corporeal systems. *Int. Res. J. Biol. Sci.* **2013**, *2*, 18–29.
  51. Mcfeeters, S.K. The use of the normalized difference water index (NDWI) in the delineation of open water

- features. *Int. J. Remote Sens.* **1996**, *17*, 1425–1432.
52. Chuvieco, E.; Ventura, G.; Martín, M.P.; Gómez, I. Assessment of multitemporal compositing techniques of MODIS and AVHRR images for burned land mapping. *Remote Sens. Environ.* **2005**, *94*, 450–462.
53. Huete, A.; Didan, K.; Miura, T.; Rodriguez, E.P.; Gao, X.; Ferreira, L.G. Overview of the radiometric and biophysical performance of the MODIS vegetation indices. *Remote Sens. Environ.* **2002**, *83*, 195–213.



© 2017 by the authors. Submitted for possible open access publication under the terms and conditions of the Creative Commons Attribution (CC BY) license (<http://creativecommons.org/licenses/by/4.0/>).